University of Glasgow

DEPARTMENT OF

AEROSPACE ENGINEERING

Far-Field Boundary Conditions for Solutions to the Navier-Stokes Equations

B.Gribben, K.J.Badcock and B.E.Richards

Aerospace Engineering Departmental Report No. 9324

August 6, 1993

Far-Field Boundary Conditions for Solutions to the Navier-Stokes Equations

B.Gribben, K.J.Badcock and B.E.Richards
Aerospace Engineering Departmental Report No. 9324
August 6, 1993

Abstract

The effect of reducing the extent of the computational domain for transonic lifting flow over an aerofoil in an unbounded domain is examined. A correction to the far field boundary conditions is developed based on a far field expansion of the linearized small-disturbance equation. Improved accuracy is demonstrated on smaller computational domains.

CONTENTS

1 Introduction

The evolution of the discipline of computational fluid dynamics (CFD) in the past few decades has gone hand in hand with the rapid growth of available computer power. CFD enables the solution by numerical methods of fluid dynamics problems which are intractable by analytical methods. The now widespread use of the Euler and Navier-Stokes equations as the governing equations in CFD as opposed to simpler fluid models [1] is a measure of the growing maturity of the discipline. CFD has now become a fundamental element of the modern aerospace design process together with wind tunnel and flight testing. The principal use of CFD is to predict the nature of the flow, often involving complex flow phenomena, around proposed geometries and hence contribute to geometry optimisation of both major and minor components.

The use of panel methods to solve linearised potential flow equations [2] was initially demonstrated by Hess and Smith [3] in 1962. Steady improvement of potential schemes resulted in the first applications of CFD to aircraft design in the late 1960's, notably in the configuration development and aeroelastic analysis in the U.S. supersonic transport programme. Accurate lift and lift-curve slope predictions were achieved but pressure distribution calculations were unsatisfactory. In later years increasingly complex and successful potential methods were developed. The fact that the computing power is now available to tackle the more complete and mathematically involved Euler/Navier-Stokes formulations does not mean that methods considering less complex flow physics are obsolete. Potential models are often perfectly adequate and offer the considerable advantage of requiring greatly reduced computer power and hence cost for implementation. Comparitible run times and costs for a range of solution methods is presented in Appendix 3. Considerable aerodynamic improvements were made to the Bell V-22 Osprey tilt rotor vehicle in the mid 1980's by including in the design process CFD methods employing relatively simple flow models. 3-D panel methods were employed to redesign the wing/fuselage fairing in order to avoid flow separation in the forward region of the fairing. CFD was also crucial to the design of the flaps, spinner and nacelle inlets. However, for more complex flowfields potential methods are not valid. There has been an increasing demand within the aircraft industry for applications codes which use the Euler/Navier-Stokes formulation for evaluating flowfields such as those associated with propulsion/airframe integration, large scale separation, multiple lifting surface interactions, shock waves, high angle of attack flowfield prediction, performance boundary prediction, and flutter and buffet calculations where unsteady boundary-layer separation is present. Major breakthroughs were MacCormack's explicit difference scheme in 1970 [4] and the implicit scheme of Beam and Warming in 1976 [5]. Considerable effort has been devoted to Euler/Navier-Stokes schemes since the early 1980's resulting in advances in accuracy and speed, but robustness and generality have proved elusive; these schemes require special skill to run successfully and nearly always require a supercomputer, which compares unfavourably with the wide range of potential method design tools which can be run by non-expert CFD users on high-end personal

computers. Despite this drawback, Euler schemes have been employed with increasing success to many design problems. For example, Euler codes have been used in recent years by Boeing for the analysis of advanced propfan aircraft [6][7] where the main problem is power-induced interference effects on the aerodynamics of the aircraft. Another example of the successful application of Euler codes is described in references [8] and [9] where the effect of tractor mounted propfans on the wing pressure distribution was accurately predicted. The calculation of the NASA Space Shuttle ascent environment, see pages 863-886 of reference [1], represents one of the few actual design applications of Navier-Stokes schemes to date. The results were used to provide a new source of information in the transonic and supersonic regime, which resolved inconsistencies in the existing aerodynamic loads data base acquired through wind tunnel and flight testing. These calculations require six hours of CPU time on a Cray 2, which is adequate explanation in itself as to why Navier-Stokes code applications are as yet not widely employed as design tools. A brief cost analysis comparing Cray YMP and workstation usage is included in Appendix 4.

In recent years there have been significant advances in methods for Navier-Stokes equations. Modern computers make Navier-Stokes calculations practical, although improvements are constantly being sought to reduce the required computer power. In this study the efficient use of an existing Navier-Stokes code is examined and an improvement to the code is developed. Both these considerations have the same aim, to reduce the problem complexity and computing time.

When an aerofoil is placed in a uniform stream, the effect of the presence of the aerofoil on the flow extends to infinite distances from the aerofoil. However, in CFD it is common to consider a computational domain whose extent is just great enough to enable the assumption of uniform freestream conditions outwith the domain, in the far field, to yield acceptably accurate solutions for the problem being considered. The size of the computational domain has to be restricted as much as possible to enable a fast computer solution. In this report the effect of varying the extent of the computational domain or far field distance is examined in an attempt to determine an optimum trade-off between accuracy and speed.

Also considered is a method of obtaining a more accurate solution by introducing a far field boundary correction. An improvement upon the assumption of freestream conditions at the boundary of the computational domain can be achieved by solving exactly a simpler set of equations for the flow in the far field and using this solution to provide the far field conditions for the full simulation. It is then possible to significantly reduce the boundary extent yet still attain satisfactory results.

The tests were performed using the Glasgow University turbulent flow solver, an existing code integrating the full Navier-Stokes equations, see equations 11 in Appendix 1. The thin-layer form of the non-dimensionalised equations is solved in general curvilinear coordinates. The non-dimensionalisation is with respect to freestream temperature, Mach number and velocity. To summarise the solution procedure, the convective terms are discretised by Osher's approximate

Riemann Solver [10] with a MUSCL interpolation [11] providing 2nd or 3rd order accuracy. When a limiter is required in the following, the Van Albada limiter [12] is used. The viscous terms are centrally differenced and Riemann invariants are used to impose far field boundary conditions. The explicit method can be written in the form

$$w^{n+1} = w^n - \frac{\Delta t}{\Delta x} R_s\left(w^n\right)$$

where R_s denotes the steady residual obtained from the discretisation, and w is the first vector in equations (N-S).

Calculations were made using two C-type meshes:

Grid	Dimensions	Cells on surface	Far field location (chord lengths)
1	136x36	104	30
2	256x64	208	10

Flow solutions are presented for the RAE 2822 aerofoil. Experimental transonic case 9 of reference [13] is considered. Aerofoil design data and wind tunnel model characteristics are listed in Appendix 2. Detailed model geometry is included in reference [13].

The development of the boundary conditions is discussed in the following section, section 2. In section 3 it is described how the influence of the boundary extent on the calculations was examined. In section 4 the far field boundary correction is introduced and its effect is evaluated. The results are presented and discussed in section 5.

2 Characteristic Treatment at the Boundary

The method of characteristics is used to obtain the far field boundary conditions. A local coordinate system (x,y) is constructed on the outer boundary, with x normal to and directed outward from the the outer boundary, and y tangential to the boundary. If it is assumed that derivatives along the boundary can be neglected, ie $\partial/\partial y = 0$, then it is possible to apply a quasi-one-dimensional characteristic analysis to obtain far field boundary conditions. The basis of this analysis is the unsteady Euler equation, (equation 12 of Appendix 1):

$$\frac{\partial \underline{U}}{\partial t} + \frac{\partial \underline{F}}{\partial x} = 0$$

$$\text{where } \underline{U} = \begin{bmatrix} \rho \\ \rho u \\ \rho v \\ \rho e \end{bmatrix} \text{ and } \underline{F} = \begin{bmatrix} \rho u \\ \rho u^2 + p \\ \rho u v \\ \rho u\left(e + \frac{p}{\rho}\right) \end{bmatrix}$$

This models a two-dimensional flow with gradients only in the x direction. It is possible to rewrite this equation in the form

$$\frac{\partial \underline{U}}{\partial t} + \underline{A}\frac{\partial \underline{U}}{\partial x} = 0 \qquad \text{where } \underline{A} \text{ is the Jacobian matrix } \frac{\partial \underline{F}}{\partial \underline{U}} \tag{1}$$

The derivation of the Jacobian is facilitated by introducing a new set of variables u_1, u_2, u_3, u_4:

$$\underline{U} = \begin{bmatrix} \rho \\ \rho u \\ \rho v \\ \rho e \end{bmatrix} = \begin{bmatrix} u_1 \\ u_2 \\ u_3 \\ u_4 \end{bmatrix}$$

By using the equations

$$p = (\gamma - 1)\rho i \qquad i : \text{internal energy per unit mass}$$

$$\rho i = \rho e - \frac{1}{2}\rho\left(u^2 + v^2\right) \qquad \gamma : \text{ratio of specific heats}$$

it is possible to show that

$$\underline{F} = \begin{bmatrix} u_2 \\ \dfrac{u_2^2}{u_1} + (\gamma - 1)\left[u_4 - \dfrac{1}{2}\left(\dfrac{u_2^2}{u_1} + \dfrac{u_3^2}{u_1}\right)\right] \\ \dfrac{u_2 u_3}{u_1} \\ \dfrac{u_2 u_4}{u_1} + \dfrac{u_2}{u_1}(\gamma - 1)\left[u_4 - \dfrac{1}{2}\left(\dfrac{u_2^2}{u_1} + \dfrac{u_3^2}{u_1}\right)\right] \end{bmatrix}$$

By simple differentiation it is then possible to determine the Jacobian matrix:

$$\underline{A} = \begin{bmatrix} 0 & 1 & 0 & 0 \\ \left(\frac{\gamma-3}{2}\right)u^2 + \left(\frac{\gamma-1}{2}\right)v^2 & (3-\gamma)u & (1-\gamma)v & \gamma-1 \\ -uv & v & u & 0 \\ -\gamma u\, e + (\gamma-1)\left(u^2+v^2\right)u & \gamma e - \left(\frac{\gamma-1}{2}\right)\left(3u^2+v^2\right)u & (1-\gamma)uv & \gamma u \end{bmatrix}$$

By applying a characteristic analysis to the four equations in (1) it is possible to obtain four equations in (x -t) space which may be used to determine the far field boundary conditions. The matrix $\underline{A}$ can be expressed as

$$\underline{A} = \underline{E}\underline{\Lambda}\underline{E}^{-1} \qquad (2)$$

where $\underline{\Lambda} = \begin{bmatrix} u & 0 & 0 & 0 \\ 0 & u+a & 0 & 0 \\ 0 & 0 & u-a & 0 \\ 0 & 0 & 0 & u \end{bmatrix}$

The diagonal terms of $\underline{\Lambda}$ are the eigenvalues of $\underline{A}$. $\underline{E}$ is a matrix whose columns are the right eigenvectors of $\underline{A}$. $\underline{E}^{-1}$ is the inverse of $\underline{E}$ and is a matrix whose rows are the left eigenvectors of $\underline{A}$. Combining (1) and (2) it can be shown that

$$\underline{E}^{-1}\frac{\partial \underline{U}}{\partial t} + \underline{\Lambda}\underline{E}^{-1}\frac{\partial \underline{U}}{\partial x} = 0$$

The four resulting equations are

$$\frac{\partial s}{\partial t} + u\frac{\partial s}{\partial x} = 0 \qquad (3)$$

$$\frac{\partial R^+}{\partial t} + (u+a)\frac{\partial R^+}{\partial x} - \frac{a}{\gamma(\gamma-1)}\left[\frac{\partial s}{\partial t} + (u+a)\frac{\partial s}{\partial x}\right] = 0 \qquad (4)$$

$$\frac{\partial R^-}{\partial t} + (u-a)\frac{\partial R^-}{\partial x} - \frac{a}{\gamma(\gamma-1)}\left[\frac{\partial s}{\partial t} + (u-a)\frac{\partial s}{\partial x}\right] = 0 \qquad (5)$$

$$\frac{\partial v}{\partial t} + u\frac{\partial v}{\partial x} = 0 \qquad (6)$$

where $R^+ = u + 2a/(\gamma-1)$ and $R^- = u - 2a/(\gamma-1)$

s is the entropy obtained from $s = \ln(p/\rho^\gamma)$

a is the local sonic velocity obtained from $a^2 = \gamma p/\rho$

In the far field the flow may be considered to be homentropic since there are no discontinuities such as shock waves. Equations (4) and (5) then reduce to:

$$\frac{\partial R^+}{\partial t} + (u + a)\frac{\partial R^+}{\partial x} = 0 \qquad (7)$$

$$\frac{\partial R^-}{\partial t} + (u - a)\frac{\partial R^-}{\partial x} = 0 \qquad (8)$$

From equations (3), (6), (7) and (8) the following characteristic equations may be constructed:

$$\frac{ds}{dt} = 0 \quad \text{along } C^0: \ \frac{dx}{dt} = u \qquad \frac{dv}{dt} = 0 \quad \text{along } C^0: \ \frac{dx}{dt} = u$$

$$\frac{dR^+}{dt} = 0 \quad \text{along } C^+: \ \frac{dx}{dt} = u + a \qquad \frac{dR^-}{dt} = 0 \quad \text{along } C^-: \ \frac{dx}{dt} = u - a$$

The quantities s, v, R^+, R^-, are referred to as Riemann invariants since they are constant along the characteristic directions $dx/dt = u, u, u+a, u-a$ respectively. Fig.1 shows the characteristic paths for subsonic outflow, $0 < u < a$.

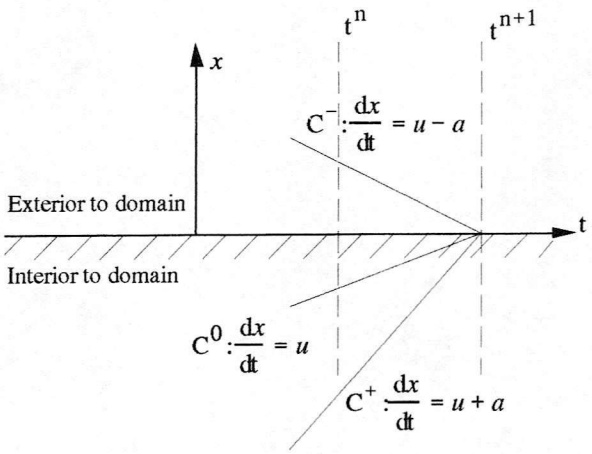

Fig. 1 Characteristic paths at far field boundary

Whether each Riemann invariant is extrapolated from the exterior or the interior of the computational domain depends on whether the characteristic is incoming or outgoing. If the flow across the boundary is subsonic, two types of boundary can be distinguished:

1. Subsonic outflow see Fig. 1.

   $u > 0, u + a > 0, u - a > 0$ therefore s, v, R^+ are extrapolated from the interior, R^- from the exterior.

2. Subsonic inflow

   $u < 0, u + a > 0, u - a < 0$ therefore s, v, R^- are extrapolated from the exterior, R^- from the interior.

In practice, the interior of the domain is taken to be the cell centre adjacent to the boundary. Conditions exterior to the domain are taken as freestream conditions when a far field representation is absent. Including the far field boundary corrections discussed in section 6 enables improved modelling of the conditions exterior to the domain by accommodating perturbation velocity terms arising from a point vortex representation of the aerofoil.

3 Effect of Reducing Far Field Distance

To examine the effect of the boundary extent of the computational domain on the calculations, three approaches were adopted:

1. Decreasing the boundary extent of grid 1 from 31 to 4.976 chord lengths in the downstream direction, see Figs. 2.
2. Decreasing the boundary extent of grid 1 from 30 to 2.087 chord lengths in the upstream/crosstream direction, see Figs. 3.
3. Decreasing the boundary extent of grid 2 from 10.75 to 2.556 chord lengths in the upstream/crosstream direction, see Figs. 4.

In all three cases, the boundary extent was reduced by dropping successive grid lines from the outer boundary of the full grid. It is evident from the results obtained that the prediction of lift, drag and pressure distribution deteriorates as the size of the computational domain is decreased. In the next section it is described how an improvement was made to the code to make the accuracy of the calculations less dependent on the boundary extent. The results are discussed in full in section 5.

4 Effect of Far Field Boundary Correction

The far-field boundary correction is based on the assumption that the behaviour of the flow in the far-field is consistent with the Prandtl-Glauert equation, developed in Appendix 1:

$$\left(1 - M_\infty^2\right)\phi_{xx} + \phi_{yy} = 0$$

where M_∞ represents the freestream Mach number, ϕ denotes the velocity potential, and x and y represent the distances along and normal to the freestream velocity respectively.

Define a new velocity potential

$$\phi'(x',y') = \beta^2\phi(x,y) \qquad \text{where} \quad x' = x \quad y' = \beta y \quad \beta^2 = 1 - M_\infty^2 \quad \Gamma = \Gamma'/\beta^2$$

By the chain rule

$$\frac{\partial\phi}{\partial x} = \frac{\partial\phi}{\partial x'}\frac{\partial x'}{\partial x} + \frac{\partial\phi}{\partial y'}\frac{\partial y'}{\partial x}$$

$$= \frac{\partial\phi}{\partial x'}.1 + \frac{\partial\phi}{\partial y'}.0 = \frac{\partial\phi}{\partial x'} = \frac{1}{\beta^2}\frac{\partial\phi'}{\partial x'}$$

$$\frac{\partial\phi}{\partial y} = \frac{\partial\phi}{\partial x'}\frac{\partial x'}{\partial y} + \frac{\partial\phi}{\partial y'}\frac{\partial y'}{\partial y}$$

$$= \frac{\partial\phi}{\partial x'}.0 + \frac{\partial\phi}{\partial y'}.\beta = \beta\frac{\partial\phi}{\partial y'} = \frac{1}{\beta}\frac{\partial\phi'}{\partial y'}$$

$$\text{ie} \quad u = \frac{u'}{\beta^2} \qquad \text{ie} \quad v = \frac{v'}{\beta}$$

and applying the chain rule again gives

$$\frac{\partial^2\phi}{\partial x^2} = \frac{1}{\beta^2}\frac{\partial^2\phi'}{\partial x'^2} \qquad \frac{\partial^2\phi}{\partial y^2} = \frac{\partial^2\phi'}{\partial y'^2}$$

Substituting into the Prandtl-Glauert equation yields

$$\phi'_{x'x'} + \phi'_{y'y'} = 0$$

The far field perturbation velocities can then be represented as a Laurent series about the origin.

$$u' = \sum_{n=1}^{\infty}\frac{1}{r'^n}\left[b'_n\cos(n\theta') + c'_n\sin(n\theta')\right] \qquad (9)$$

$$v' = \sum_{n=1}^{\infty}\frac{1}{r'^n}\left[b'_n\cos(n\theta') + c'_n\sin(n\theta')\right] \qquad (10)$$

The symbols r' and θ' denote the radius and polar angle in the transformed plane. The coefficients b'_n and c'_n can be evaluated from thin aerofoil theory as

$$b'_n = \frac{1}{2\pi}\int_0^c \sigma' x^{n-1} dx \qquad n = 1,\infty$$

$$c'_n = \frac{1}{2\pi}\int_0^c \omega' x^{n-1} dx \qquad n = 1,\infty$$

where c is the chord length, σ is the source strength and ω is the vorticity. The leading terms of (9) and (10) decrease as the inverse of the radial distance in the transformed plane. Since the other terms decrease as the inverse of the square (at least) of the radial distance they are assumed negligibly small at the far field. For the leading term

$$b'_1 = 0 \qquad c'_1 = \frac{\Gamma'}{2\pi}$$

since vorticity integrated along the chord length is equal to the circulation strength. Substituting these into (9) and (10) gives

$$u' = \frac{1}{r'}\frac{\Gamma'}{2\pi}\sin\theta'$$

and noting that

$$r' = \sqrt{x'^2 + y'^2} \qquad \sin\theta' = \frac{y'}{\sqrt{x'^2 + y'^2}}$$

$$\Gamma' = \beta^2\Gamma \qquad x' = x \qquad y' = \beta y$$

gives the perturbation velocity in the transformed plane:

$$u' = \frac{\Gamma\beta^3}{2\pi}\frac{y}{\left(x^2 + \beta^2 y^2\right)}$$

Remembering that $u = u'/\beta^2$ to transform to the physical plane, and similarly for v:

$$u = \frac{\Gamma}{2\pi}\frac{\beta y}{\left(x^2 + \beta^2 y^2\right)} \qquad v = -\frac{\Gamma}{2\pi}\frac{\beta y}{\left(x^2 + \beta^2 y^2\right)}$$

These perturbation velocities can be combined with the freestream velocity and rotated into a body-orientated basis to obtain the corrected total velocities U and V in the far field:

$$U / q_\infty = \cos\alpha + F\sin\theta$$

$$V / q_\infty = \sin\alpha - F\cos\theta$$

$$\text{where} \quad F \equiv (c_l c / 4\pi)(\beta / r)\left[1 - M_\infty^2 \sin^2(\theta - \alpha)\right]^{-1}$$

The symbols q_∞, c_l, c, and α represent the freestream dynamic pressure, lift coefficient, aerofoil chord length and the angle of attack respectively.

The program was amended as discussed above, using the far field representation to update the far field boundary conditions. The effect of the boundary extent on the calculations using the amended code was examined by decreasing the boundary extents of grids 1 and 2 in the upstream/crosstream direction from maximums of 30 and 10.75 chord lengths respectively. The results obtained using the corrected code showed an improvement on those using the original code, and are discussed in full below.

5 Discussion and Results

The pressure distribution obtained using the full grid 1, see Fig. 3e, agrees very well with the experimental data everywhere except around the suction peak at the leading edge where the match is somewhat disappointing. The results taken as a whole indicate that the failure to accurately capture the suction peak is due to insufficient mesh density near the aerofoil. A very good match to the experimental data was achieved using the full finer mesh, see Fig. 4e. Apportioning blame to an insufficient boundary extent is ruled out since if this was the case a far larger improvement than that achieved would be expected by increasing the boundary extent from 10 to 30 chord lengths or including the far field boundary correction. Excessive numerical dissipation due to insufficient mesh density is therefore the most likely cause of the inaccuracies using grid 1.

Figs. 2a and 2b show the the change in lift and drag coefficient caused by varying the downstream boundary extent as a percentage difference from the value obtained using the full grid in each case. The gradients of the curves in the larger boundary extent region is virtually zero which suggests that the values obtained using the full grid would not be significantly improved upon by further increasing the boundary extent.

The tolerable levels of inaccuracy in predicting the lift and drag depend on the specific application. The typical values considered here are 1.5% in the lift and 0.5% in the drag. From Figs. 2a and 2b it is evident that the downstream boundary extent using the coarser mesh can be reduced to 9 chord lengths and still satisfy the lift accuracy criterion, or 17 chord lengths for the drag criterion.

Figs. 3a, 3b, 4a and 4b show that the inclusion of a far field boundary correction significantly improves the lift prediction at reduced boundary extents. Using the correction, the far field distance may be reduced to 15 chord lengths, an improvement of 2.7 on the uncorrected case for grid 1, see Fig. 3b. The effect of the correction using the fine mesh, grid 2, is similar. Referring to figure 4b, the far field distance may be reduced to 7.2 chord lengths, an improvement of 0.8 on the uncorrected case. These reductions in domain extent amount to similar reductions in computational effort since the grid density increases with aerofoil proximity.

It is difficult to gauge the effect of the correction on the drag prediction. For grid 1 the effect seems to be significant, see Fig. 3c, but for the finer grid 2 which should yield more accurate results, see Fig. 4c, the corrected and uncorrected curves actually diverge. This is not entirely unexpected since the continual problem facing even modern CFD analyses is accurate drag prediction. This casts some doubt over the validity of any conclusions drawn from Fig. 2b.

The pressure distribution achieved for the full grid 2, Fig. 4e is exceptionally good especially around the problem leading edge suction peak, and is an improvement on the results obtained by J.J. Benton [14], where a central-difference method was used. The amount by which the boundary extent may be reduced and yet still yield acceptable pressure distribution results is again dependent on the intended application. However, the graphs presented indicate that it is possible to reduce the computational domain and still obtain good results, especially with the inclusion of the far field correction. The gradual deterioration of the calculated pressure distribution can clearly be seen in Figs. 3e-h for grid 1 and 4e-h for grid 2. The improvement caused by the boundary correction becomes larger as the boundary extent is decreased. Significant errors in the pressure distribution using for example the fine mesh and the correction were not encountered until the boundary extent was reduced to the region of five chord lengths. At this proximity the shock wave begins to impinge on the boundary, therefore the original boundary conditions based on freestream conditions are invalid. The shock wave on the upper aerofoil surface is clearly seen in Fig. 5. Flow across shock waves experiences a change in entropy, therefore the boundary conditions based on the far field model where the flow is assumed to be homentropic are also invalid. An unexpected feature seen in Figs. 3h, 4g and 4h is that the pressure distribution around the trailing edge is worse for the case where compressible circulation at the boundary has been included. This may also be due to the breakdown of the assumptions inherent in the boundary conditions.

The improvement to the lift coefficient and pressure distribution prediction due to the inclusion of the far field boundary correction is worthwhile when it is considered that the actual amendment to the original code amounted to only six or seven lines. The possibility of further increases in efficiency by adding to the number of terms in the far field expansion as suggested by Wubs et al [15] merits further investigation.

Fig. 2a Effect of downstream boundary extent on lift coefficient, grid 1

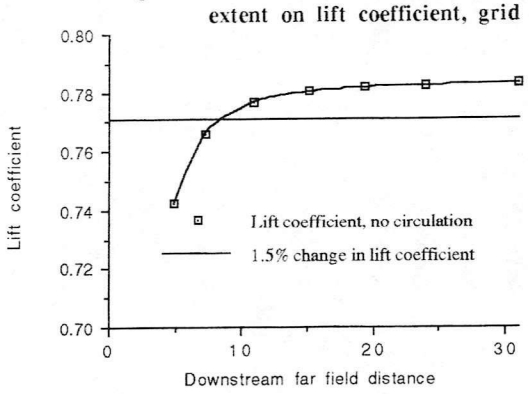

Fig. 2b Effect of downstream boundary extent on drag coefficient, grid 1

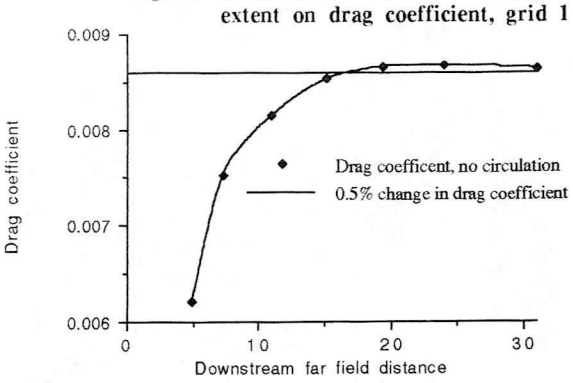

Fig. 3a Effect of upstream/crosstream boundary extent on lift coefficient, grid 1

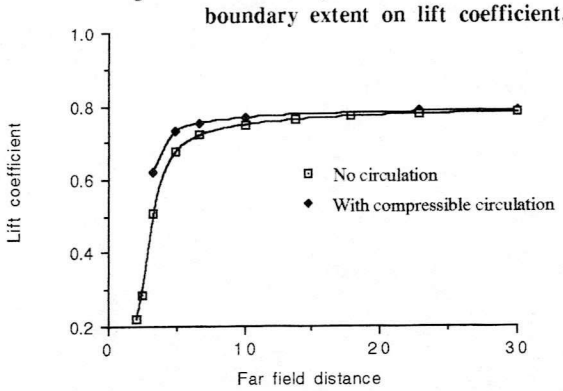

Fig. 3b % Change in lift coefficient with upstream/crosstream boundary extent

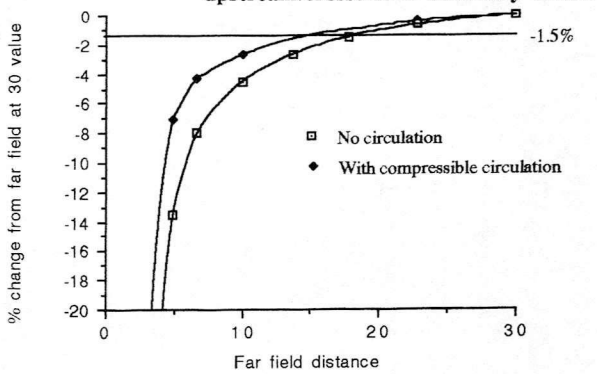

Fig. 3c Effect of upstream/crosstream boundary extent on drag coefficient, grid 1

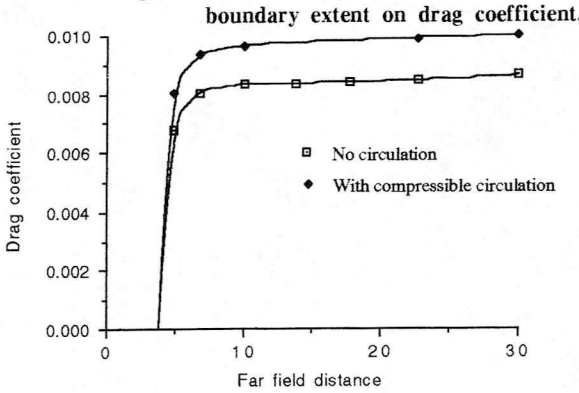

Fig. 3d % Change in drag coefficient with upstream/crosstream boundary extent

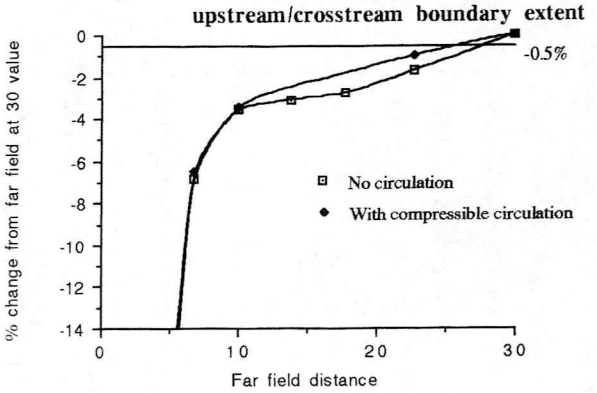

Fig. 3e Pressure distribution, grid 1
Far field distance 30 chord lengths

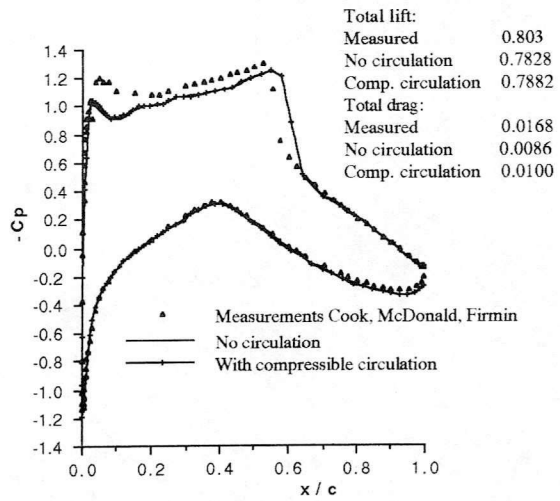

Fig. 3f Pressure distribution, grid 1
Far field distance 10 chord lengths

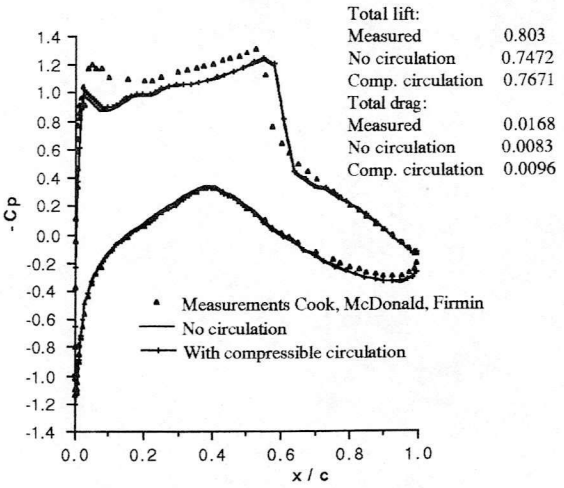

Fig. 3g Pressure distribution, grid 1
Far field distance 4.861 chord lengths

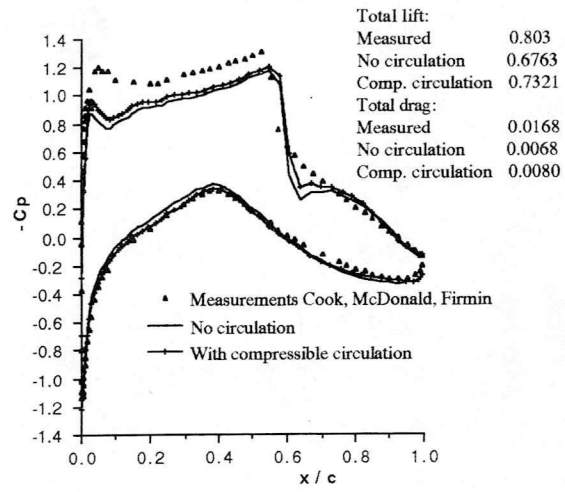

Fig. 3h Pressure distribution, grid 1
Far field distance 3.276 chord lengths

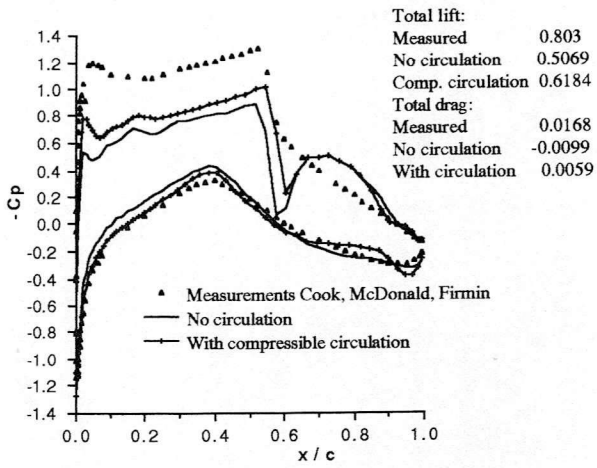

Fig. 4a Effect of upstream/crossstream boundary extent on lift coefficient, grid 2

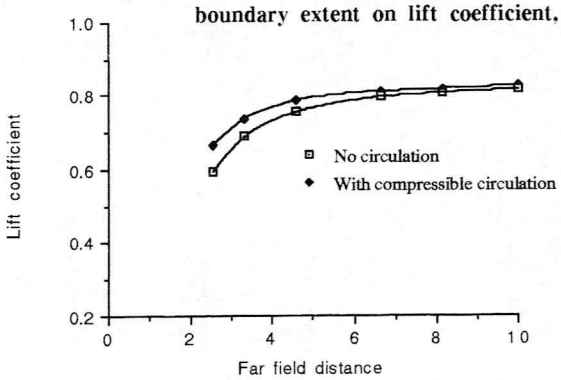

Fig. 4b % Change in lift coefficient with upstream/crosstream boundary extent

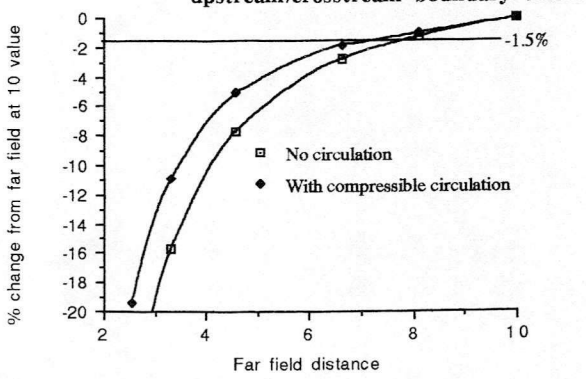

Fig. 4c Effect of upstream/crossstream boundary extent on drag coefficient, grid 2

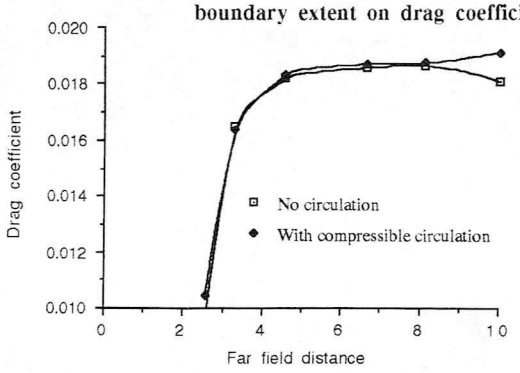

Fig. 4d % Change in drag coefficient with upstream/crossstream boundary extent

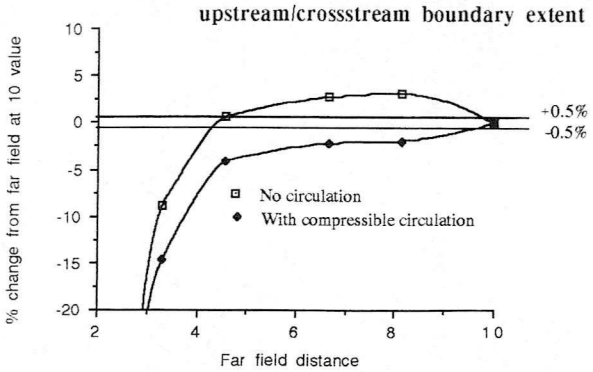

Fig. 4e Pressure distribution, grid 2
Far field distance 10 chord lengths

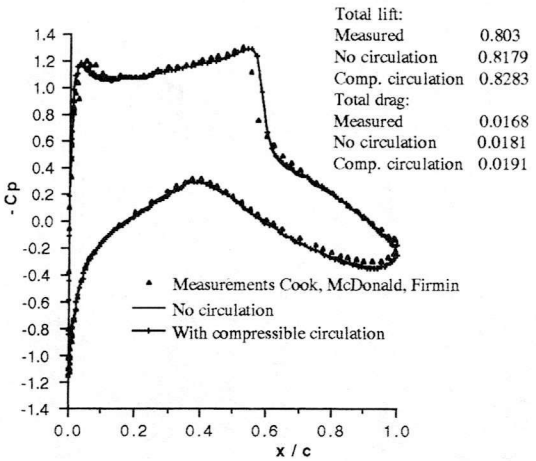

Fig. 4f Pressure distribution, grid 2
Far field distance 6.640 chord lengths

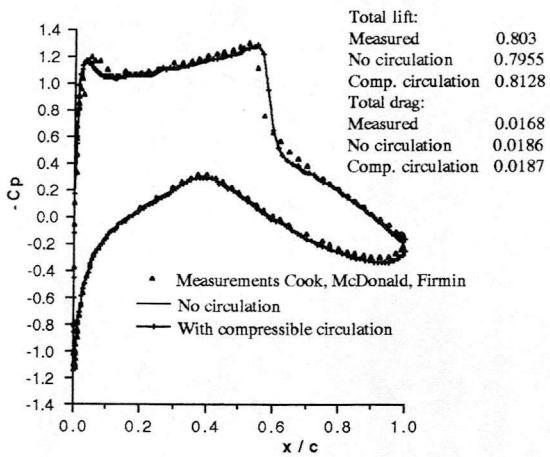

Fig. 4g Pressure distribution, grid 2
Far field distance 3.308 chord lengths

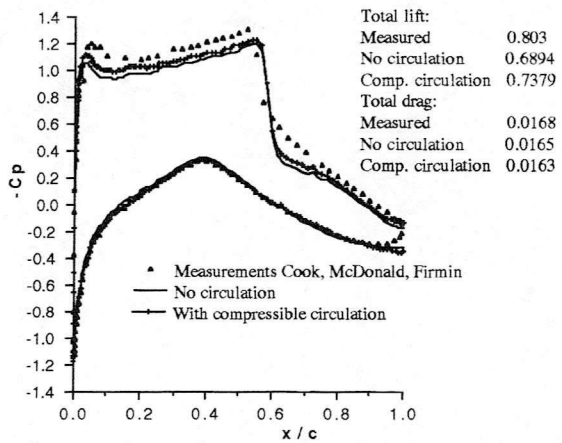

Fig. 4h Pressure distribution, grid 2
Far field distance 2.556 chord lengths

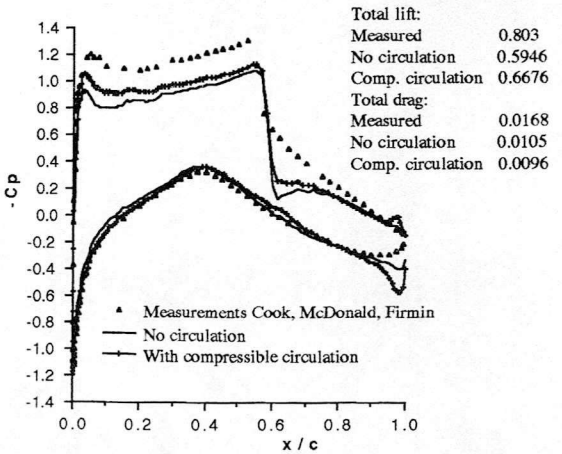

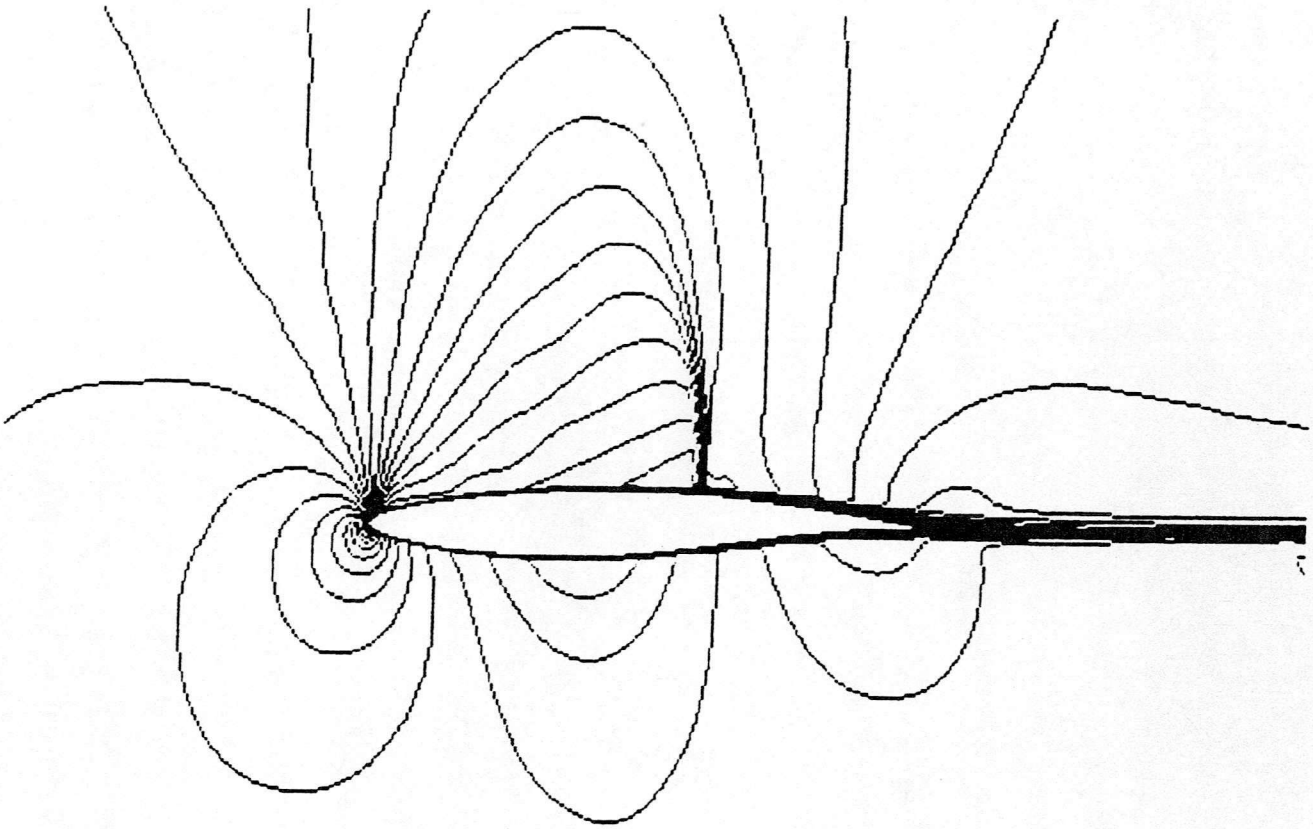

Fig. 5 Mach number distribution around RAE 2822 aerofoil showing shock wave on upper surface

References

[1] P.A.Henne (editor),"Applied Computational Aerodynamics," *Progress In Astronautics and Aeronautics*, AIAA Inc., Washington D.C., Vol. 125, 1990.

[2] J.D.Anderson,"Fundamentals of Aerodynamics,"McGraw-Hill, New York, 1984.

[3] J.L.Hess and A.M.O.Smith,"Calculation of Non-Lifting Potential Flow About Arbitrary Three-Dimensional Bodies,"*Douglas Aircraft Rept.* ES 40622, 1962.

[4] R.W.MacCormack,"The Effect of Viscosity in Hyper-Velocity Impact Cratering,"*AIAA Paper* 69-354, 1969.

[5] R.W.Beam and R.F.Warming,"An Implicit Finite Difference Algorithm for Hyperbolic Systems in Conservative Form,"*J. Comp. Phys.*, 23: 87-110, 1976.

[6] N.J.Yu, K.Kusunose, H.C.Chen and D.M.Summerfield,"Flow Simulations for a Complex Airplane Configuration Using Euler Equations,"*AIAA Paper* 87-0454, Jan. 1987.

[7] K.Kusunose, D.L.Marcum, H.C.Chen and N.J.Yu,"Transonic Analysis For Complex Airplane Configurations,"*AIAA Paper* 87-1196, June 1987.

[8] N.J.Yu, S.S.Samant and P.E.Rubbert,"Flow Predictions for Propfan Configurations Using Euler Equations,"*AIAA Paper* 84-1645, June 1984.

[9] N.J.Yu and H.C.Chen,"Flow simulations for Nacelle-Propeller Configurations Using Euler Equations,"*AIAA Paper* 84-1645, June 1984.

[10] S.Osher and S.R.Chakravarthy, "Upwind schemes and boundary conditions with applications to Euler equations in general coordinates,"*J. Comp. Phys.*, 50: 447-481, 1983.

[11] B.Van Leer,"Towards the ultimate conservative difference scheme via second-order sequel to Godunov's method,"*J. Comp, Phys.*,32:101-136, 1979.

[12] B.Van Leer, G.D.Van Albada and W.W.Roberts,"A comparative study of computational methods in cosmic gas dynamics," *Astronomy and Astrophysics*, 108, 1982.

[13] P.H.Cook, M.A.McDonald, M.C.P.Firmin,"Aerofoil RAE2822 – Pressure Distributions, and Boundary Layer and Wake Measurements,"*RAE Tech Memo Aero 1275*, Sept 1977.

[14] J.J.Benton,"Validation of 2-D Navier-Stokes Codes with respect to Turbulence Modelling: Aerofoil RAE 2822 Cases 9 and 10,"*British Aerospace Final Report*, Feb 1992.

[15] F.W.Wubs, J.W.Boerstoel and A.J.Van Der Wees,"Grid Size Reduction in Flow Calculations on Infinite Domains by Higher Order Far-Field Asymptotics in Numerical Boundary Conditions,"*Journal of Engineering Mathematics*, Vol.18,1984, pp.157-177.

[16] J.W.Edwards and J.B.Malone,"Current Status of Computational Methods for Transonic Unsteady Aerodynamics and Aeroelastic Applications,"*AGARD Conference Proceedings 507 Transonic Unsteady Aerodynamics and Aeroelasticity*, March 1992.

[17] R.Radespiel, C.Rossow and R.C.Swanson,"Efficient Cell-Vertex Multigrid Scheme for Three-Dimensional Navier-Stokees Equations,"*AIAA Journal*, Vol. 28, No.8, August 1990.

Appendix 1: The Prandtl-Glauert Equation

The two-dimensional laminar Navier-Stokes equations in conservative form are given by:

$$\frac{\partial}{\partial t}\begin{bmatrix}\rho\\ \rho u\\ \rho v\\ \rho e\end{bmatrix}+\frac{\partial}{\partial x}\begin{bmatrix}\rho u\\ \rho u^2+p\\ \rho uv\\ \rho u\left(e+\frac{p}{\rho}\right)\end{bmatrix}+\frac{\partial}{\partial y}\begin{bmatrix}\rho v\\ \rho vu\\ \rho v^2+p\\ \rho v\left(e+\frac{p}{\rho}\right)\end{bmatrix}-\mu\left[\frac{\partial}{\partial x}\begin{bmatrix}0\\ \tau_{xx}\\ \tau_{xy}\\ u\tau_{xx}+v\tau_{xy}\end{bmatrix}+\frac{\partial}{\partial y}\begin{bmatrix}0\\ \tau_{xy}\\ \tau_{yy}\\ u\tau_{xy}+v\tau_{yy}\end{bmatrix}\right]-k\left[\frac{\partial^2}{\partial x^2}\begin{bmatrix}0\\ 0\\ 0\\ T\end{bmatrix}+\frac{\partial^2}{\partial y^2}\begin{bmatrix}0\\ 0\\ 0\\ T\end{bmatrix}\right]=0 \tag{11}$$

The symbols ρ, u, v, p, μ, k, T, represent the fluid density, the two components of velocity, pressure, viscosity, heat conductivity, and temperature respectively. The symbol e denotes the total internal energy per unit mass, given by

$$e = c_v T + \frac{1}{2}\left(u^2 + v^2\right)$$

where the constant c_v denotes the specific heat at constant volume.

The Euler equations can be obtained by assuming that viscous effects are negligible:

$$\frac{\partial}{\partial t}\begin{bmatrix}\rho\\ \rho u\\ \rho v\\ \rho e\end{bmatrix}+\frac{\partial}{\partial x}\begin{bmatrix}\rho u\\ \rho u^2+p\\ \rho uv\\ \rho u(e+\frac{p}{\rho})\end{bmatrix}+\frac{\partial}{\partial y}\begin{bmatrix}\rho v\\ \rho vu\\ \rho v^2+p\\ \rho v(e+\frac{p}{\rho})\end{bmatrix}=0 \tag{12}$$

If the flow is assumed to be steady, the time dependent term is equal to zero, yielding the momentum and continuity equations:

$$u\frac{\partial u}{\partial x}+v\frac{\partial u}{\partial y}=-\frac{1}{\rho}\frac{\partial p}{\partial x}$$

$$u\frac{\partial v}{\partial x}+v\frac{\partial v}{\partial y}=-\frac{1}{\rho}\frac{\partial p}{\partial y}$$

$$\frac{\partial \rho u}{\partial x}+\frac{\partial \rho v}{\partial y}=0$$

If it is assumed that the flow is isentropic then the relationship $a^2=dp/d\rho$ may be used, where a is

the local sonic velocity, and after some manipulation these three equations may be arranged to give:

$$\left(\frac{u^2}{a^2}-1\right)\frac{\partial u}{\partial x}+\frac{uv}{a^2}\left(\frac{\partial u}{\partial y}+\frac{\partial v}{\partial x}\right)+\left(\frac{v^2}{a^2}-1\right)\frac{\partial v}{\partial y}=0$$

If the irrotationality condition

$$\left(\frac{\partial v}{\partial x}-\frac{\partial u}{\partial y}\right)=0$$

is introduced, along with the velocity potential function ϕ, then the above equation becomes

$$\left(\frac{u^2}{a^2}-1\right)\frac{\partial^2\phi}{\partial x^2}+\left(\frac{2uv}{a^2}\right)\frac{\partial^2\phi}{\partial x\partial y}+\left(\frac{v^2}{a^2}-1\right)\frac{\partial^2\phi}{\partial y^2}=0$$

This can be rewritten in terms of only one dependent variable, ϕ:

$$\left[1-\frac{1}{a^2}\left(\frac{\partial\phi}{\partial x}\right)^2\right]\frac{\partial^2\phi}{\partial x^2}-\frac{2}{a^2}\left(\frac{\partial\phi}{\partial x}\right)\left(\frac{\partial\phi}{\partial y}\right)\frac{\partial^2\phi}{\partial x\partial y}+\left[1-\frac{1}{a^2}\left(\frac{\partial\phi}{\partial y}\right)^2\right]\frac{\partial^2\phi}{\partial y^2}=0 \qquad (13)$$

Consider a thin body placed in a uniform stream of velocity V_∞ such that

$$\phi_x = u'+V_\infty \qquad \phi_y = v' \qquad \phi_z = w'$$

where u', v', and w' are the perturbation velocity components. Substituting these into (13) gives:

$$\left(\frac{V_\infty^2+2u'V_\infty+u'^2}{a^2}-1\right)\phi_{xx}+2\left(\frac{V_\infty v'+u'v'}{a^2}\right)\phi_{xy}+\left(\frac{v'^2}{a^2}\right)\phi_{yy}=0$$

For isentropic flow, the energy relation can be written in the form:

$$a^2+\frac{1}{2}(\gamma-1)V^2=a_\infty^2+\frac{1}{2}(\gamma-1)V_\infty^2$$

If the velocity is written as the sum of free stream and perturbation parts in this equation, the local sonic ratio can be written as

$$\left(\frac{a}{a_\infty}\right)^2=1-\frac{\gamma-1}{2}M_\infty^2\left(2\frac{u'}{V_\infty}+\frac{u'^2}{V_\infty^2}+\frac{v'^2}{V_\infty^2}\right) \qquad (14)$$

If it is assumed that the perturbation velocity components are small compared to the freestream velocity, then higher order terms in the perturbation to freestream ratio may be neglected:

$$\left(\frac{a}{a_\infty}\right)^2 \approx 1-(\gamma-1)M_\infty^2\frac{u'}{V_\infty}$$

By combining the above equation with equation (14) and neglecting all terms in the parentheses of second order in the perturbations it can be shown that

$$\left[\left(M_\infty^2-1\right)+(\gamma+1)M_\infty^2\frac{\phi_x}{V_\infty}\right]\phi_{xx}+\left(2M_\infty^2\frac{\phi_y}{V_\infty}\right)\phi_{xy}-\phi_{yy}=0$$

For slender bodies it is possible to neglect the middle term since the lateral velocity perturbation is small:

$$\left[\left(M_\infty^2-1\right)+(\gamma+1)M_\infty^2\frac{\phi_x}{V_\infty}\right]\phi_{xx}-\phi_{yy}=0$$

In flows other than in near sonic flows (ie for Mach numbers less than 0.8 and greater than 1.2) the absolute value of the first term in the parentheses is much greater than the second term, which may be neglected. This yields the first order transonic small perturbation or Prandtl-Glauert equation:

$$\left(1-M_\infty^2\right)\phi_{xx}+\phi_{yy}=0$$

This equation is only valid under specific flow conditions, summarised below:

- No body forces act on the flow
- Viscous effects are negligible
- Flow is steady, isentropic and irrotational
- Chord-wise perturbation velocity component dominates
- Flow Mach numbers are outwith transonic region.

Appendix 2: Aerofoil Description and Test Data

Aerofoil

Designation	RAE 2822
Type	Subcritical, rear loaded, rooftop type design pressure
Nose radius	0.00827 chord
Max. thickness	0.121 chord

Design condition:

Freestream Mach no.	0.66
Lift coefficient	0.56
Incidence	1.06 degrees

Model geometry:

Chord	0.61 m
Exposed span	1.83 m
Max. thickness	73.76 mm
Base thickness	0.06 mm
Aspect ratio	3

Test Data

Wind tunnel:

RAE Farnborough

8ft x 6ft transonic continuous closed circuit type

Test case 9 conditions:

Freestream Mach no.	0.73
Incidence	3.19 degrees
Reynold's no.	6.5 million
Transition trip	0.03 chord
Tunnel height / aerofoil chord ratio	4

Test case 9 measurements:

Lift coefficient	0.803
Drag coefficient	0.0168
Pitching moment coefficient (0.25 chord)	-0.099

Appendix 3: Comptational Resource Estimates

Listed below are run times and running costs on a Cray 2/YMP for increasingly complex solution methods. Estimates are for high speed, low angle conditions around a single half-span wing up to "locally separating" flow. Values taken from reference [16].

		TSD	TSD-Visc	Euler	TLNS	TLNS-Radespiel
Algorithm speed (μsec/grid point/step)		3	6.2	60	65	65
Number of steps:	Steady State	1000	1000	1000	5000	460
	Dynamic	7	7	7	7	
	Steady State/Dynamic	300	300	300	1000	
Number of grid points (Kilopoints)		200	400	240	650	920
Run time Cray 2/YMP (hrs)						
	Steady state	0.17	0.69	4.00	58.68	7.661
	Dynamic	0.35	1.45	8.40	82.15	
Cost @ $100 per hour per node		35	145	840	8,215	766

Solution Method

TSD : Transonic small disturbance
TSD-Visc : Transonic small disturbance with interacted boundary layer model
TLNS : Thin-Layer Navier-Stokes
TLNS-Radespiel : Multigrid method Thin-Layer Navier-Stokes solver [17].

It is clearly shown that increasing the complexity of the governing equations for the solution method requires a substantial increase in run time and hence cost. The inclusion of the TLNS-Radespiel method also demonstrates that large reductions in cost are possible even with Navier-Stokes methods by using improved codes.

Appendix 4: The Economics of High Performance Computing

Basic Information			
Exchange rate ($ per £)	**1.5**		
Bytes/word	**8**		
No of hours in year	**8,760**		
Specification of CRAY YMP			
No. of Processors	**8**		
CPU rate per processor (Megaflops)	**333**		
Memory per processor (Mwords)	**128**		
Cost per hour per node ($ per hour)	**100**		
Overall CPU rate (Megaflops)	2,664		
Overall memory (Mwords)	1,024		
Cost per year (£) (academic rates - info from RAL)	4,672,000		
Specification of Workstation (predicted 1994 technology)			
CPU rate per workstation (Megaflops)	**100**		
Memory per workstation (Mbytes)	**256**		
Cost per workstation (£)	**10,000**		
Cost of Site Software Licences (one off)	**10,000**		
Expected lifespan	**3**		
Workstation Cluster equivalent to CRAY YMP			
No. of workstations to make a CRAY	26.64		
Memory of clustered workstations (Mwords)	852		
Capital Cost £	276,400		
Cost £ per year	92,133		
Comparison			
Annual cost YMP/Annual cost Equivalent Cluster	50.71		
Memory CRAY/ Memory Equivalent Workstations	1.20		
High Performance Computer Using multiple Workstations			
No of workstations?	**8**	**32**	**64**
Overall CPU rate (Megaflops)	800	3,200	6,400
Overall memory (Mwords)	256	1,024	2,048
Capital Cost £	90,000	330,000	650,000
Cost £ per year	36,667	116,667	223,333

Note:
The CRAY YMP costs are based on academic rates supplied by Rutherford Appleton Laboratory.
The 1994 Workstation specifications are predicted from current development trends.
A CRAY YMP can only be accessed through a workstation.

The relatively small annual cost of the Workstation cluster compared with the Cray YMP suggests that Workstation cluster development will become increasingly important in the future.